Article

Evaluation of an Image-Derived Input Function for Kinetic Modeling of Nicotinic Acetylcholine Receptor-Binding PET Ligands in Mice

Matthew Zammit [1,†], Chien-Min Kao [1,†], Hannah J. Zhang [1], Hsiu-Ming Tsai [1], Nathanial Holderman [1], Samuel Mitchell [1], Eve Tanios [1], Mohammed Bhuiyan [1], Richard Freifelder [1], Anna Kucharski [1,2], William N. Green [3,4,‡], Jogeshwar Mukherjee [5,‡] and Chin-Tu Chen [1,*,‡]

[1] Department of Radiology, University of Chicago, Chicago, IL 60637, USA
[2] Fermi National Accelerator Laboratory, Batavia, IL 60510, USA
[3] Department of Neurobiology, University of Chicago, Chicago, IL 60637, USA
[4] Marine Biological Laboratory, Woods Hole, MA 02543, USA
[5] Department of Radiological Sciences, University of California, Irvine, CA 92697, USA
[*] Correspondence: c-chen@uchicago.edu; Tel.: +1-773-702-6269
[†] These authors contributed equally to this work.
[‡] These authors equally supervised this work.

Abstract: Positron emission tomography (PET) radioligands that bind with high-affinity to $\alpha4\beta2$-type nicotinic receptors ($\alpha4\beta2$Rs) allow for in vivo investigations of the mechanisms underlying nicotine addiction and smoking cessation. Here, we investigate the use of an image-derived arterial input function and the cerebellum for kinetic analysis of radioligand binding in mice. Two radioligands were explored: 2-[^{18}F]FA85380 (2-FA), displaying similar pKa and binding affinity to the smoking cessation drug varenicline (Chantix), and [^{18}F]Nifene, displaying similar pKa and binding affinity to nicotine. Time–activity curves of the left ventricle of the heart displayed similar distribution across wild type mice, mice lacking the $\beta2$-subunit for ligand binding, and acute nicotine-treated mice, whereas reference tissue binding displayed high variation between groups. Binding potential estimated from a two-tissue compartment model fit of the data with the image-derived input function were higher than estimates from reference tissue-based estimations. Rate constants of radioligand dissociation were very slow for 2-FA and very fast for Nifene. We conclude that using an image-derived input function for kinetic modeling of nicotinic PET ligands provides suitable results compared to reference tissue-based methods and that the chemical properties of 2-FA and Nifene are suitable to study receptor response to nicotine addiction and smoking cessation therapies.

Keywords: kinetic modeling; nicotine; addiction; PET; Nifene; 2-FA85380

1. Introduction

Tobacco use is the leading cause of preventable deaths in the United States and one of the prominent causes of nicotine addiction [1]. Nicotine permeates the blood–brain barrier and binds to high-affinity nicotinic acetylcholine receptors (nAChRs) containing $\alpha4$ and $\beta2$ subunits ($\alpha4\beta2$Rs) [2]. Chronic exposure to nicotine causes upregulation of $\alpha4\beta2$Rs, in which increases in both the density of high-affinity binding sites and the functional response of $\alpha4\beta2$Rs are observed [3–6]. In addition, the process of nicotine-induced $\alpha4\beta2$R upregulation has been linked to nicotine addiction [7,8].

Nicotine, and other weak-base ligands of $\alpha4\beta2$Rs, such as the smoking cessation drug varenicline (Chantix), rapidly reach equilibrium in intracellular organelles and concentrate in acidic organelles [9,10]. The high pKa and binding affinity of varenicline causes selective trapping of this ligand inside intracellular acidic vesicles containing high-affinity $\alpha4\beta2$Rs [10]. Alternatively, nicotine concentrates inside these acidic vesicles but does not

become trapped due to its lower pKa and lower binding affinity and is rapidly released from the vesicles [10]. Nicotine-induced upregulation increases the number of high-affinity binding sites within the acidic vesicles and increases the number of acidic vesicles, allowing for the vesicles to trap varenicline in higher concentrations. Recently, our in vitro studies suggest these acidic vesicles to be Golgi satellites (GSats), a novel intracellular compartment in neurons and neuronal dendrites that contain high α4β2R density, which increase in number following exposure to nicotine [10,11]. While nicotine and varenicline bind to the same α4β2Rs, the residence time of nicotine in the brain is 1–2 h, compared to the 4–5-day residence time of varenicline, which may be attributed to varenicline trapping inside GSats. It has been shown that dissipating the pH gradient across GSats with chloroquine diphosphate or ammonium chloride prevents trapping of varenicline in GSats, and under these conditions, exposure to varenicline results in similar α4β2R upregulation as observed with nicotine [10]. Cell pretreatment with chloroquine diphosphate or ammonium chloride did not affect the extent of α4β2R upregulation induced by nicotine exposure.

Of interest is to monitor the effects of nicotine addiction and smoking cessation in vivo. This can be achieved using positron emission tomography (PET), in which the binding of nicotinic ligands to α4β2Rs can be observed noninvasively through injection of nanomolar concentrations of radiolabeled nicotine analogs [12]. Initial PET studies imaged [^{11}C]nicotine; however, this ligand suffered from rapid dissociation of the receptor–ligand complex, high levels of nonspecific binding, and its accumulation in the brain was highly dependent on cerebral blood flow [13–15]. The radioligand 2-[^{18}F]FA85380 (2-FA) was developed as a less toxic analog of epibatidine that overcomes the shortcomings of [^{11}C]nicotine and binds with high affinity to α4β2Rs [16], but requires a prolonged imaging session to achieve accurate quantification [17]. [^{18}F]Nifene was then developed as a ligand with moderate affinity to α4β2Rs to improve upon the slow kinetics of 2-FA [18]. Since the slow kinetics of 2-FA closely resemble epibatidine and varenicline, and the fast kinetics of Nifene resemble nicotine, these ligands can be used to monitor the mechanisms of smoking cessation and nicotine addiction in vivo. Our previous in vitro findings with these ligands found that chronic exposure to Nifene resulted in similar α4β2R upregulation as observed with nicotine, whereas exposure to 2-FA did not cause upregulation, similar to varenicline [10]. The high pKa and high affinity of 2-FA likely result in the same GSat trapping observed with varenicline, and pH dissipation across GSats with chloroquine diphosphate or ammonium chloride prevented 2-FA trapping and caused significant α4β2R upregulation following exposure to 2-FA. This phenomenon was also observed in vivo using PET, in which mice pretreated with chloroquine diphosphate showed reduced binding of 2-FA, while Nifene binding was unaffected [10].

One challenge associated with PET quantification of 2-FA and Nifene is the lack of a suitable reference tissue due to the abundance of α4β2Rs in the brain. Typically, the cerebellum is chosen as a reference tissue due to its low uptake and rapid washout of α4β2R-binding radioligands. In nonhuman primates, the cerebellum was validated as a suitable reference tissue for α4β2R-binding radioligands [17]; however, in rodents, radioligand concentrations in the cerebellum can be displaced by nicotine or lobeline injection [19], indicative of some specific binding signal. Human imaging studies incorporated the corpus collosum as a reference tissue; however, this needs to be further validated using a nicotine challenge to measure the nicotine displaceable component [18]. It is speculated that the corpus collosum may be a suitable reference tissue free of specific binding in rodents, but partial volume effects may negatively affect quantification in this region due to its small volume and the low spatial resolution of PET. Due to the lack of a true tissue reference region for rodent imaging, studies incorporating the cerebellum as a reference tissue likely underestimate the true binding potential. Apart from performing arterial cannulation to measure the input function, use of an image-derived input function for kinetic radioligand analysis is speculated as a noninvasive alternative to improve image quantification [20]. Studies incorporating image-derived input functions have shown that the time-activity

curve (TAC) from the left ventricle of the heart was an accurate representation of arterial blood, obviating the need for arterial cannulation [21–25].

Here, we provide an exploratory analysis of the use of the left ventricle as an image-derived input function without arterial sampling for quantification of 2-FA and Nifene PET images of mice, as well as use of the cerebellum as a tissue reference region. As preclinical PET images of rodents encompass the entire animal body within the scanner field of view, obtaining a TAC from the left ventricle is feasible for kinetic PET analyses. This study is the first to explore use of an image-derived input function for the quantification of nicotinic PET ligands in preclinical mouse models. Left ventricle TACs were compared between wild type, β2-knockout, and acute nicotine-treated mice to explore how different mouse models influence radioligand activity concentration in the blood pool. Using a two-tissue compartment model fit (2TCM) of the PET data, rate constants of radioligand association and dissociation were calculated to determine the radioligand binding potential. Binding potential values were then directly compared against estimates derived using the cerebellum reference tissue previously explored for these radioligands. Finally, 2TCM fit simulations were performed to assess the stability of the rate constant estimates using the left ventricle TAC input function.

2. Results

2.1. Left Ventricle Comparisons

2-FA and Nifene time-activity curves (TACs) of the left ventricle, thalamus, midbrain, and cerebellum for all mice are provided in Figure 1a. For 2-FA, peak SUVs in the left ventricle (presented as mean (SD)) for WT mice (0.55 (0.17)), KO mice (0.47 (0.22)), and AN mice (0.569 (0.12)) showed no significant differences (ANOVA F(df): 0.62(2); *p*-value: 0.54; η^2: 0.05 [0.00, 0.23]). Mean SUVs from the final 30 min data frames of WT mice (0.077 (0.029)), KO mice (0.081 (0.049)), and AN mice (0.074 (0.014)) showed no significant differences (ANOVA F(df): 0.75(2); *p*-value: 0.93; η^2: 0.006 [0.00, 0.0071]). For Nifene, peak SUVs in the left ventricle (presented as mean (SD)) for WT mice (0.98 (0.21)), KO mice (1.4 (0.95)), and AN mice (1.2 (0.15)) showed no significant differences (ANOVA F(df): 1.38 (2); *p*-value: 0.27; η^2: 0.11 [0.00, 0.32]). Mean SUVs from the final 30 min data frames of WT mice (0.41 (0.14)), KO mice (0.45 (0.14)), and AN mice (0.50 (0.12)) showed no significant differences (ANOVA F(df): 0.64(2); *p*-value: 0.54; η^2: 0.05 [0.00, 0.22]).

2.2. Binding Potential Comparisons

Using the left ventricle TAC as an input to the 2TCM, BP_{ND} values were calculated for the thalamus, midbrain, and cerebellum of WT, KO, and AN mice by taking the ratio of k_3 and k_4 (Figure 1b). From ANOVA with post hoc Tukey's HSD, 2-FA BP_{ND} values were significantly higher in the thalamus, midbrain, and cerebellum of WT mice compared to KO and AN mice (*p* < 0.05), while no significant difference was observed between KO and AN mice (*p* > 0.05). For Nifene, BP_{ND} values were significantly higher in the thalamus, midbrain, and cerebellum of WT mice compared to KO and AN mice (*p* < 0.05), while no significant difference was observed between KO and AN mice (*p* > 0.05).
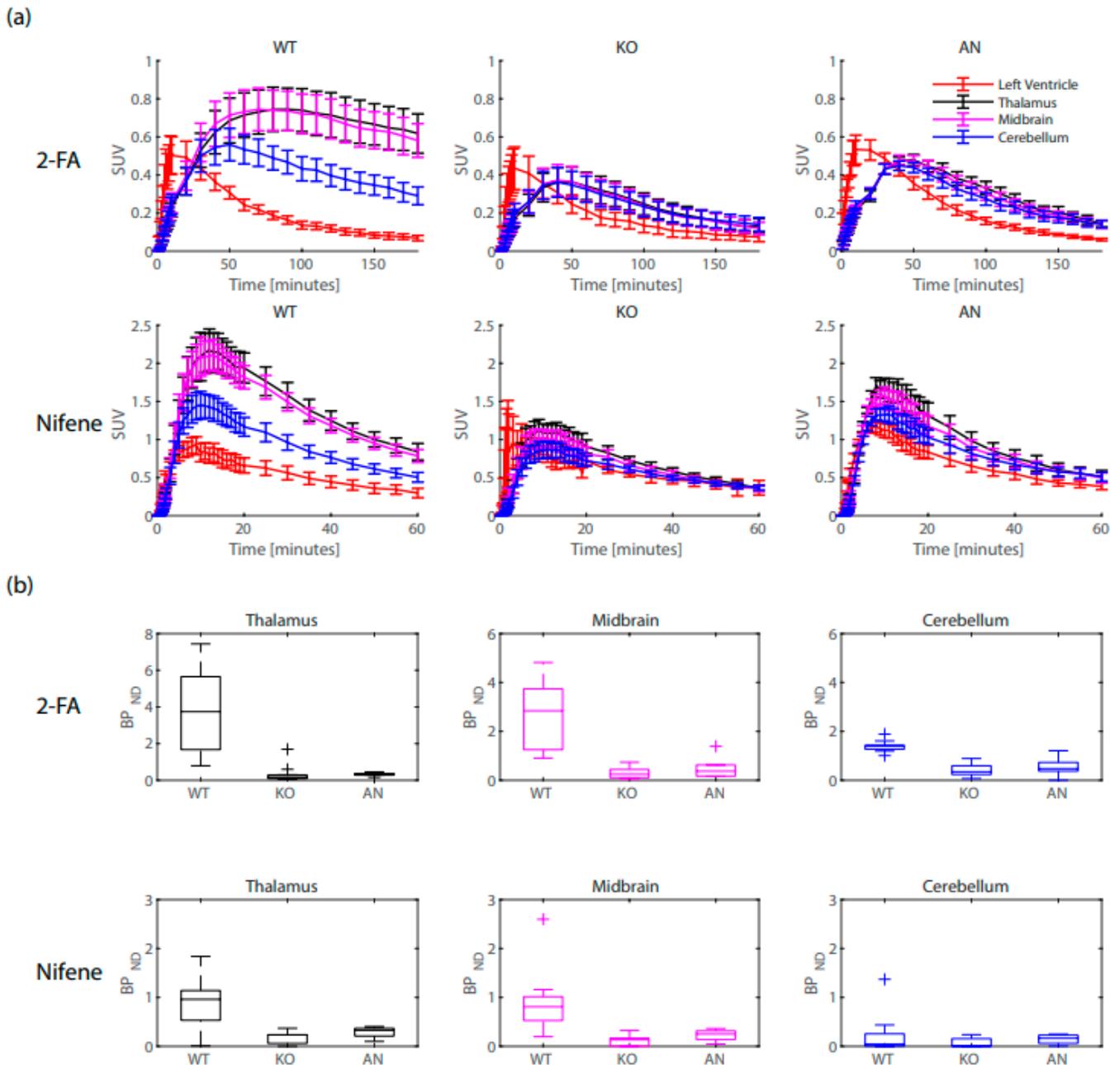
Figure 1. (**a**) 2-FA and Nifene standardized uptake value (SUV) time-activity curves (TACs) for WT, KO, and AN mice. Error bars represent the standard deviation. (**b**) 2-FA and Nifene BP_{ND} values for the thalamus (black), midbrain (magenta) and cerebellum (blue) of WT, KO, and AN mice.

2.3. 2TCM Rate Constants

Table 1 provides the rate constant estimates with ANOVA F-statistics and effect size estimates (η^2 with 95% CIs) from the 2TCM for the thalamus and midbrain imaged with 2-FA and Nifene. For 2-FA, significant differences were observed between WT, KO, and AN mice for K_1 values in the thalamus, but not the midbrain. No significant differences were observed with k_2 values in both the thalamus and midbrain across all groups. Significant differences between groups for both regions were observed for k_3 and k_4 values. Post hoc Tukey's HSD revealed that the WT mice had higher estimates of k_3 and lower estimates of k_4 compared to KO and AN mice. In addition, Tukey's HSD revealed no significant difference in k_3 and k_4 values between KO and AN mice. For Nifene, significant differences were observed between mice for K_1 values in the thalamus and midbrain. From Tukey's

HSD, the significance was driven by the comparison between WT and KO mice. KO and AN mice and WT and AN mice showed no significant difference between K_1 estimates. No significant difference in k_2 values were observed between mice in the thalamus, but midbrain k_2 values were significantly different. For the midbrain, k_2 values in WT mice were significantly higher than in the KO mice, and no differences were observed between the other pairings of mice. Significant difference in k_3 values were observed between mice in the thalamus and midbrain. For both the thalamus and midbrain, no significant differences were observed for k_4 values between mice.

Table 1. Rate constants for WT, KO, and AN mice imaged with 2-FA and Nifene with ANOVA statistics and effect size (η^2) estimates with 95% Cis.

Radioligand	Region	Rate Constant (1/min)	WT	KO	AN	ANOVA F(df)	*p*-Value	η^2
2-FA	Thalamus	K_1	0.098 (0.013)	0.066 (0.0061)	0.060 (0.0036)	3.88(2)	0.035	0.24 [0.00, 0.45]
		k_2	0.075 (0.015)	0.055 (0.0066)	0.050 (0.0046)	1.37(2)	0.27	0.10 [0.00, 0.31]
		k_3	0.029 (0.0064)	0.0049 (0.0016)	0.0054 (0.00080)	9.75(2)	0.00080	0.45 [0.11, 0.62]
		k_4	0.0077 (0.0013)	0.020 (0.0037)	0.016 (0.0017)	5.48(2)	0.011	0.31 [0.02, 0.51]
	Midbrain	K_1	0.11 (0.017)	0.076 (0.0087)	0.062 (0.0051)	2.67(2)	0.090	0.18 [0.00, 0.39]
		k_2	0.076 (0.020)	0.066 (0.0087)	0.051 (0.0055)	0.54(2)	0.59	0.04 [0.00, 0.21]
		k_3	0.024 (0.0062)	0.0060 (0.0012)	0.0031 (0.00070)	6.70(2)	0.0049	0.36 [0.05, 0.55]
		k_4	0.0084 (0.0016)	0.026 (0.0037)	0.0093 (0.0022)	11.70(2)	0.00029	0.49 [0.16, 0.65]
	Cerebellum	K_1	0.10 (0.016)	0.077 (0.0072)	0.063 (0.0053)	2.53(2)	0.10	0.17 [0.00,0.39]
		k_2	0.080 (0.016)	0.068 (0.0069)	0.058 (0.0057)	0.68(2)	0.52	0.05 [0.00, 0.23]
		k_3	0.011 (0.0025)	0.0056 (0.00083)	0.0036 (0.0010)	4.29(2)	0.026	0.26 [0.00, 0.47]
		k_4	0.0081 (0.0017)	0.017 (0.0040)	0.015 (0.0059)	1.534(2)	0.24	0.11 [0.00, 0.31]
Nifene	Thalamus	K_1	1.66 (0.24)	0.55 (0.089)	1.25 (0.072)	7.82(2)	0.0027	0.42 [0.08, 0.60]
		k_2	1.23 (0.26)	0.51 (0.074)	1.09 (0.068)	3.05(2)	0.068	0.22 [0.00, 0.44]
		k_3	0.43 (0.11)	0.047 (0.011)	0.14 (0.024)	4.96(2)	0.017	0.31 [0.01, 0.52]
		k_4	0.50 (0.12)	0.27 (0.034)	0.51 (0.12)	1.71(2)	0.20	0.13 [0.00, 0.35]
	Midbrain	K_1	1.94 (0.31)	0.50 (0.080)	1.28 (0.099)	8.00(2)	0.0024	0.42 [0.08, 0.60]
		k_2	1.52 (0.35)	0.47 (0.069)	1.14 (0.061)	3.54(2)	0.047	0.24 [0.00, 0.46]
		k_3	0.50 (0.13)	0.029 (0.0085)	0.12 (0.026)	5.75(2)	0.0098	0.34 [0.03, 0.54]
		k_4	0.60 (0.14)	0.26 (0.046)	0.60 (0.077)	2.21(2)	0.13	0.17 [0.00, 0.39]
	Cerebellum	K_1	1.56 (0.33)	0.33 (0.061)	0.91 (0.10)	5.19(2)	0.014	0.32 [0.02, 0.52]
		k_2	1.19 (0.32)	0.31 (0.053)	0.83 (0.072)	2.81(2)	0.082	0.20 [0.00, 0.42]
		k_3	0.10 (0.055)	0.010 (0.0052)	0.033 (0.013)	1.21(2)	0.32	0.10 [0.00, 0.31]
		k_4	0.62 (0.18)	0.19 (0.046)	0.34 (0.14)	2.00(2)	0.16	0.16 [0.00, 0.37]

2.4. Rate Constant Comparisons between In-House Python Solver and PMOD Solver

Table 2 displays the 2-FA rate constant estimates from the Python and PMOD 2TCM solvers, and the pairwise *t*-test comparisons between them. For WT mice, there were no significant differences between estimates of K_1, k_2, k_3, or k_4 in the thalamus or midbrain between methods. PMOD estimates for K_1, k_3, and k_4 were significantly higher than the Python solver in KO mice, and PMOD estimates for k_3 and k_4 were higher in AN mice. Since KO and AN mice display no specific binding of 2-FA, estimates of these rate constants display high variance, which may influence the trend of higher mean values. Table 3 displays the Nifene rate constant estimates from the Python and PMOD 2TCM solvers, and the pairwise *t*-test comparisons between them. For WT mice, there were no significant differences between estimates of k_3 or k_4 in the thalamus or midbrain between methods. However, K_1 and k_2 estimates from the Python solver were significantly higher than the PMOD estimates. KO and AN mice revealed no significant differences between rate constant values in the thalamus and midbrain. Lack of Nifene-specific binding in KO and AN mice contributes to the higher variance in these measurements for the Python and PMOD solvers.

Table 2. 2-FA rate constants measured using the in-house Python solver and the PMOD solver compared using pairwise *t*-tests.

Group	Rate Constant	Region	2TCM Python	2TCM PMOD	T-Value	*p*-Value
WT	K_1	Thalamus	0.098 (0.013)	0.13 (0.022)	1.17	0.27
		Midbrain	0.11 (0.017)	0.12 (0.014)	1.23	0.25
	k_2	Thalamus	0.075 (0.015)	0.19 (0.085)	1.24	0.24
		Midbrain	0.076 (0.020)	0.13 (0.028)	1.61	0.14
	k_3	Thalamus	0.029 (0.0064)	0.071 (0.021)	1.69	0.12
		Midbrain	0.024 (0.0062)	0.043 (0.0076)	2.26	0.051
	k_4	Thalamus	0.0077 (0.0013)	0.026 (0.017)	0.98	0.35
		Midbrain	0.0084 (0.0016)	0.013 (0.0032)	1.28	0.23
	BP_{ND}	Thalamus	3.84 (0.70)	5.70 (1.25)	1.42	0.19
		Midbrain	2.66 (0.41)	3.78 (0.55)	1.94	0.084
KO	K_1	Thalamus	0.066 (0.0061)	0.14 (0.030)	2.39	0.038
		Midbrain	0.076 (0.0087)	0.18 (0.041)	2.46	0.034
	k_2	Thalamus	0.055 (0.0066)	0.44 (0.18)	1.97	0.077
		Midbrain	0.066 (0.0087)	0.54 (0.20)	2.18	0.054
	k_3	Thalamus	0.0049 (0.0016)	0.090 (0.023)	3.49	0.0059
		Midbrain	0.0060 (0.0012)	0.092 (0.027)	2.98	0.014
	k_4	Thalamus	0.020 (0.0037)	0.049 (0.0060)	5.39	0.00030
		Midbrain	0.026 (0.0037)	0.044 (0.0080)	3.02	0.013
	BP_{ND}	Thalamus	0.34 (0.14)	2.07 (0.63)	2.44	0.035
		Midbrain	0.29 (0.064)	1.92 (0.54)	2.66	0.024
AN	K_1	Thalamus	0.060 (0.0036)	0.34 (0.13)	1.85	0.12
		Midbrain	0.062 (0.0051)	0.37 (0.12)	2.26	0.073
	k_2	Thalamus	0.050 (0.0046)	1.23 (0.63)	1.71	0.15
		Midbrain	0.051 (0.0055)	1.19 (0.47)	2.20	0.079
	k_3	Thalamus	0.0054 (0.00080)	0.087 (0.023)	2.91	0.033
		Midbrain	0.0031 (0.00070)	0.085 (0.028)	2.67	0.045
	k_4	Thalamus	0.016 (0.0017)	0.030 (0.0028)	3.14	0.026
		Midbrain	0.0093 (0.0022)	0.031 (0.0024)	6.03	0.0018
	BP_{ND}	Thalamus	0.33 (0.037)	2.84 (0.86)	2.66	0.045
		Midbrain	0.52 (0.17)	2.61 (0.77)	2.77	0.039

Table 3. Nifene rate constants measured using the in-house Python solver and the PMOD solver compared using pairwise *t*-tests.

Group	Rate Constant	Region	2TCM Python	2TCM PMOD	T-Value	*p*-Value
WT	K_1	Thalamus	1.66 (0.24)	1.18 (0.13)	3.60	0.0042
		Midbrain	1.94 (0.31)	1.45 (0.17)	2.83	0.016
	k_2	Thalamus	1.23 (0.26)	0.61 (0.12)	3.37	0.0062
		Midbrain	1.52 (0.35)	0.85 (0.15)	2.33	0.040
	k_3	Thalamus	0.43 (0.11)	0.76 (0.51)	0.72	0.49
		Midbrain	0.50 (0.13)	0.36 (0.12)	0.68	0.51
	k_4	Thalamus	0.50 (0.12)	1.63 (0.62)	2.09	0.060
		Midbrain	0.60 (0.14)	1.42 (0.56)	1.77	0.10
	BP_{ND}	Thalamus	0.90 (0.14)	0.57 (0.18)	2.28	0.043
		Midbrain	0.88 (0.17)	0.63 (0.22)	1.10	0.30
KO	K_1	Thalamus	0.55 (0.089)	0.52 (0.12)	0.73	0.48
		Midbrain	0.50 (0.080)	0.50 (0.11)	0.0096	0.99
	k_2	Thalamus	0.51 (0.074)	0.63 (0.29)	0.52	0.62
		Midbrain	0.47 (0.069)	0.45 (0.098)	0.33	0.75
	k_3	Thalamus	0.047 (0.011)	0.075 (0.037)	0.62	0.55
		Midbrain	0.029 (0.0085)	0.068 (0.043)	0.87	0.41
	k_4	Thalamus	0.27 (0.034)	2.64 (1.04)	2.16	0.062
		Midbrain	0.26 (0.046)	0.65 (0.35)	1.01	0.34

Table 3. *Cont.*

Group	Rate Constant	Region	2TCM Python	2TCM PMOD	T-Value	*p*-Value
	BP_{ND}	Thalamus	0.18 (0.038)	0.030 (0.010)	4.13	0.0033
		Midbrain	0.12 (0.034)	0.11 (0.047)	0.15	0.88
AN	K_1	Thalamus	1.25 (0.072)	1.00 (0.050)	1.92	0.15
		Midbrain	1.28 (0.099)	1.25 (0.083)	0.20	0.86
	k_2	Thalamus	1.09 (0.068)	0.86 (0.15)	1.09	0.35
		Midbrain	1.14 (0.061)	1.29 (0.21)	0.57	0.61
	k_3	Thalamus	0.14 (0.024)	0.65 (0.39)	1.19	0.32
		Midbrain	0.12 (0.026)	1.37 (1.04)	1.02	0.38
	k_4	Thalamus	0.51 (0.12)	4.23 (1.73)	1.90	0.15
		Midbrain	0.60 (0.077)	3.83 (1.62)	1.80	0.17
	BP_{ND}	Thalamus	0.29 (0.056)	0.31 (0.17)	0.11	0.91
		Midbrain	0.23 (0.056)	0.40 (0.14)	0.88	0.44

2.5. 2TCM Comparisons to Logan Graphical Analysis

The 2TCM estimate of $BP_{\mathrm{ND}} + 1$ from the Python solver using a left ventricle input function was directly compared to the Logan graphical analysis estimate of DVR using a cerebellum reference tissue. Table 4 displays the pairwise comparisons between $BP_{\mathrm{ND}} + 1$ and DVR. For 2-FA, $BP_{\mathrm{ND}} + 1$ values were significantly higher than DVRs in the thalamus and midbrain of WT mice. KO and AN mice also displayed significantly higher $BP_{\mathrm{ND}} + 1$ values compared to DVR; however, the values are low and indicative of no specific binding signal. As illustrated in Figure 1b, BP_{ND} in the cerebellum of WT mice was significantly higher than observed in KO and AN mice, indicative of some 2-FA specific binding in this region. This cerebellar specific binding signal results in an underestimation of the true binding potential in the thalamus and midbrain when estimated from Logan DVR. For Nifene, no significant difference between $BP_{\mathrm{ND}} + 1$ and DVR were observed in the thalamus or midbrain of WT mice, likely because the levels of cerebellar specific binding are much lower compared to 2-FA as shown in Figure 1b and further illustrated by the SUV TACs in Figure 1a. Nifene $BP_{\mathrm{ND}} + 1$ in KO and AN mice also displayed higher values compared to DVR; however, these values are low and indicative of no radioligand specific binding.

Table 4. Pairwise comparisons between $BP_{\mathrm{ND}} + 1$ from the 2TCM and DVR from Logan graphical analysis for 2-FA and Nifene.

Radioligand	Group	Region	$BP_{\mathrm{ND}} + 1$	DVR	T-Value	*p*-Value
2-FA	WT	Thalamus	4.84 (0.70)	2.35 (0.15)	3.94	0.0034
		Midbrain	3.66 (0.41)	1.96 (0.080)	4.15	0.0025
	KO	Thalamus	1.34 (0.14)	0.97 (0.019)	2.57	0.028
		Midbrain	1.29 (0.064)	0.97 (0.011)	4.78	0.00075
	AN	Thalamus	1.33 (0.037)	1.15 (0.051)	2.73	0.042
		Midbrain	1.52 (0.17)	1.05 (0.023)	2.40	0.062
Nifene	WT	Thalamus	1.90 (0.14)	1.79 (0.079)	0.65	0.53
		Midbrain	1.88 (0.17)	1.54 (0.092)	1.82	0.095
	KO	Thalamus	1.18 (0.038)	0.94 (0.039)	5.03	0.0010
		Midbrain	1.12 (0.034)	0.98 (0.015)	3.11	0.015
	AN	Thalamus	1.29 (0.056)	0.93 (0.016)	5.79	0.010
		Midbrain	1.23 (0.056)	0.99 (0.0049)	3.57	0.037

2.6. Simulations

Simulations were performed on the PET data to evaluate the stability of the output parameters of the 2TCM fit when solved using the in-house Python solver. Briefly, the 2TCM fit was used to determine the true values of the parameters from the regional TACS from a WT, KO, and AN mouse. For each time point of the TAC, artificial noise was applied to the radioactivity concentration value with a noise level of 0.2 (noise standard deviation

relative to the amplitude) such that the noise level was proportional to the amplitude/time duration. The 2TCM fit was then applied to the noise-induced thalamus and cerebellum TACs using the noise-induced left ventricle TAC as the input function. This process was repeated over 50 iterations for each mouse and radioligand to solve for BP_{ND}, K_1, k_2, k_3, and k_4 values for the WT, KO, and AN mice. Figure 2 displays the results of the simulated 2-FA data. For the WT and KO mice, the true values of BP_{ND}, K_1, k_2, k_3, and k_4 all fell within the 25th and 75th percentile of the simulated estimates. For the AN mice, the true values of BP_{ND}, K_1, k_2, k_3, and k_4 all fell within the 25th and 75th percentile of the simulated estimates, except for the BP_{ND} of the thalamus. Figure 3 displays the results of the simulated Nifene data. For BP_{ND} values, the true values fell within the 25th and 75th percentile of the simulated estimates for the WT, KO, and AN mice. For K_1 and k_2 values, the 2TCM fit slightly underestimated the true values for all groups of mice. For k_3 and k_4 values, the true values fell within the 25th and 75th percentile of the simulated estimates for the KO and AN mice, while the WT mice simulations slightly overestimated the true values.
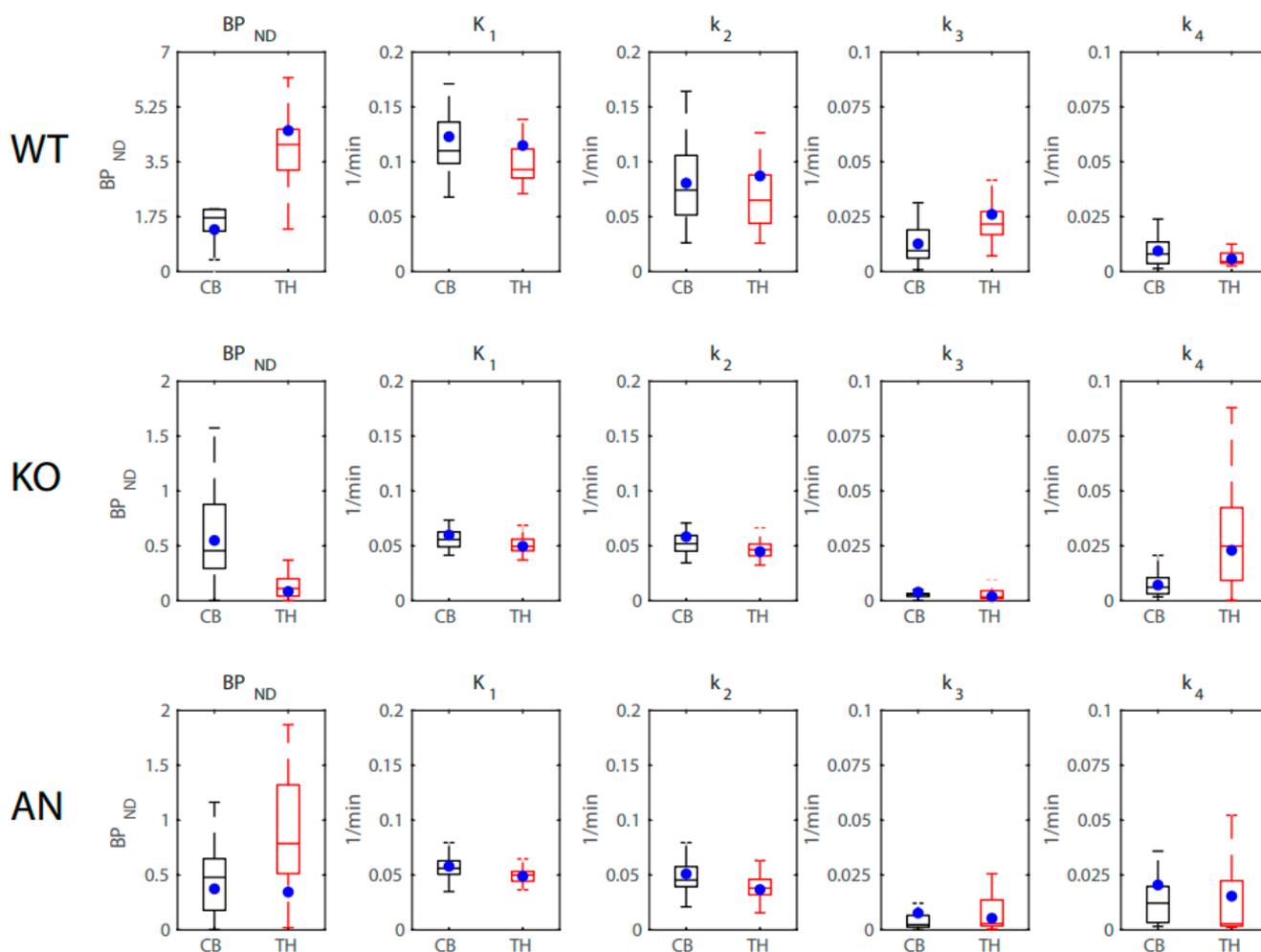

Figure 2. Distribution of simulated 2-FA BP_{ND}, K_1, k_2, k_3, and k_4 estimates from WT, KO, and AN mice in the cerebellum (CB; black) and thalamus (TH; red) using a left ventricle input function. The true values of each estimate are displayed as blue circles.
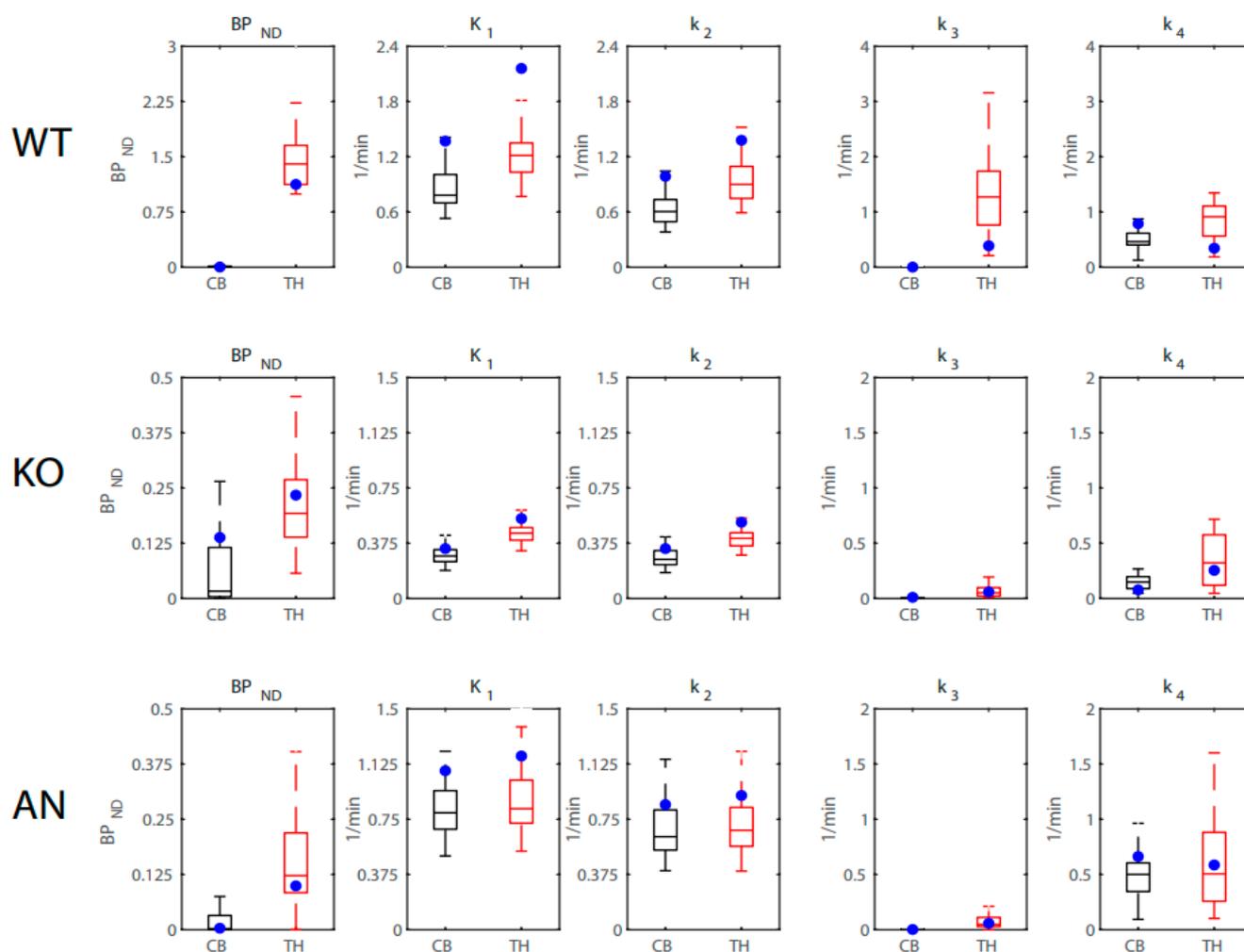
Figure 3. Distribution of simulated Nifene BP_{ND}, K_1, k_2, k_3, and k_4 estimates from WT, KO, and AN mice in the cerebellum (CB; black) and thalamus (TH; red) using a left ventricle input function. The true values of each estimate are displayed as blue circles.

3. Discussion

This study is the first to compare an image-derived input function with tissue reference region strategies for kinetic analysis of 2-FA and Nifene PET images in mice. An ROI of the left ventricle was chosen as the image-derived input function due to its accurate representation of the plasma fraction as shown in other studies [20–25], and in its current application, the left ventricle TAC showed rapid uptake and rapid clearance of 2-FA and Nifene in the blood pool. Across WT, KO, and AN mice, no differences in shape or radioactivity concentration were observed between the SUV TACs of the left ventricle, suggesting the left ventricle blood curve is stable across different mouse models studied in nicotine addiction and can be a suitable reference for these mouse models when imaging with 2-FA and Nifene. Previous studies using α4β2R PET ligands in rodents utilized the cerebellum as a tissue reference region and identified nicotine-displaceable signals in this region [19]. The current study confirms the presence of α4β2Rs in the cerebellum, notably due to the higher binding potential values of 2-FA and Nifene in the WT group compared to the KO and AN groups. Thus, studies with rodents using the cerebellum as a tissue reference region will underestimate the true binding potential in target regions of interest, further emphasizing the need for improved quantification derived from arterial data. However, the low level of specific binding in the cerebellum would only slightly underestimate the true binding potential. Importantly, DVR estimates from Logan graphical analysis using the cerebellum as a reference tissue showed lower standard deviation across

the groups of mice compared to BP_{ND} derived from the 2TCM with the image-derived input function. In clinical settings with smaller sample sizes, it may be advantageous to use brain tissue reference regions to minimize the variance across individual estimates. One limitation to our application of using an image-derived input function was delivery of the radioligands through IP injection. IP injections result in a slower distribution of radioligand from the plasma compartment to target regions when compared to the more standard IV injection. As a result, 2TCM fitting of the radioactivity time course of Nifene, which has very rapid kinetics in vivo, was challenging as the data were better represented by a 1TCM. The goodness of fit of the models, determined through the Akaike Information Criterion (AIC) confirmed that the 2TCM performed better for 2-FA (mean AIC across all mice = -988 (98)) compared to the 1TCM (AIC = -922 (143)). For Nifene, the 1TCM (AIC = -2006 (293)) outperformed the 2TCM (AIC = -1952 (303)). Compared to 2-FA, Nifene is more lipophilic and tends to concentrate in abdominal fat when injected IP, resulting in a slower plasma time course. Since the kinetics of 2-FA are very slow, use of an IP injection did not present a challenge in 2TCM fitting. Despite the challenges associated with IP injections, the 2TCM fit of the data using an image-derived input function resulted in suitable estimates of the binding potential for 2-FA, while a 1TCM fit was suitable for Nifene.

While this study is the first to assess kinetic modeling strategies of α4β2R ligands in mouse models of nicotine addiction, other studies have evaluated the kinetics in nonhuman primates [26,27]. For rhesus macaques, modeling of dynamic Nifene PET data was performed with arterial sampling and metabolite correction [26,27]. BP_{ND} values in cortical and subcortical regions of known Nifene binding were comparable between the rhesus macaques [26] and the mice used in our current study. Another study in rhesus macaques performed a 2TCM fit of the PET data with metabolite correction and found that average K_1 values for Nifene were above 1.0 (1/min), confirming the high K_1 values observed in our mouse models without arterial sampling and metabolite correction. K_1 values that exceed 1.0 (1/min) indicate complete extraction of the radioligand from plasma to tissue, consistent with what is observed with Nifene [27]. It is speculated that a transport mechanism is at play, specifically Nifene interaction with the blood–brain barrier amine transporter [28], which may account for the fast uptake rates of Nifene compared to 2-FA [27]. Similar α4β2R ligands with rapid in vivo kinetics, such as Flubatine (formerly NCFHEB), have been shown to interact with the blood–brain barrier amine transporter [29]. Furthermore, work in the field is ongoing to investigate the role of the amine transporter on Nifene passage across the blood–brain barrier [27].

The current study incorporated use of an in-house Python solver and PMOD for the 2TCM fits of the PET data. The in-house Python solver was developed to derive more stable estimates of the rate constants for the KO and AN mouse groups. Due to the low binding levels of 2-FA and Nifene in these groups, rate constant estimates using PMOD had high uncertainties. Use of parameter optimization in the Python solver greatly reduced these uncertainties in the estimates, allowing for better comparisons to the rate constants derived for the WT mice. Importantly, estimates calculated from the Python solver and PMOD were of within the same order of magnitude when fitting data from the WT mice, which displayed high levels of radioligand binding. For the WT mice, estimates of k_3 and k_4 were large for Nifene, indicative of rapid binding and unbinding from α4β2Rs. Alternatively, 2-FA showed small estimates of k_3 and very small estimates of k_4, indicative of slow binding and very slow unbinding from α4β2Rs. This very slow unbinding of 2-FA may partially be influenced by ligand trapping inside GSats, which has been shown previously in vitro and in vivo [10,11,30]. Of interest is to use these radioligands to directly study the mechanisms of nicotine addiction and smoking cessation. In vitro cellular studies performed under similar in vivo conditions in mice found that the dissociation rate of nicotine to be 0.84 1/min [31], while the dissociation rate of epibatidine was 0.043 1/min [32]. The in vivo dissociation rate (k_4) estimates of Nifene and 2-FA derived in the current study (Table 1) fall within the same order of magnitude as the in vitro estimates of nicotine and epibatidine, suggesting that these PET ligands may be useful

to study addiction and smoking cessation mechanisms, especially those involving GSat trapping and release. Because 2-FA was only imaged for a 3-h duration, a true estimate of 2-FA release from GSats could not be obtained, as radioligand did not reach equilibrium in the brain by the end of the scan. Previous in vitro work measured the dissociation of epibatidine over a 17 h duration and found that there was a rapid component (unbinding from $\alpha 4\beta 2$Rs) and a very slow component (release from GSats) [30]. Since 2-FA is an analog of epibatidine, it is speculated that this slow component of dissociation is similar between ligands and can be measured in vivo. Future work should explore whether an estimate of 2-FA release from GSats can be derived; however, the radioactive decay of F-18 may present a challenge when imaging for long scan durations. Alternatively, future studies could incorporate single-photon emission computed tomography (SPECT) scans using I-123 or I-125 labeled analogs of epibatidine to measure the release of ligand from GSats.

To directly compare to DVR estimates from tissue reference methods, $BP_{ND} + 1$ values from the 2TCM fit were compared to DVR from Logan graphical analysis [33] using a cerebellum reference tissue. For 2-FA, $BP_{ND} + 1$ was significantly higher than DVR for the thalamus and midbrain across all mouse groups. This difference is primarily due to the large BP_{ND} values present in the cerebellum, resulting in the Logan DVR underestimating the true binding potential. For Nifene, $BP_{ND} + 1$ and DVR estimates were within the same order of magnitude in the thalamus and midbrain for WT mice. This is likely because the levels of specific binding of Nifene in the cerebellum are much lower than observed with 2-FA (Figure 1b). Despite the lack of statistical significance, $BP_{ND} + 1$ values for the WT mice were higher than the observed DVR values, indicative of some levels of specific binding present in the cerebellum, resulting in DVR potentially underestimating the true binding potential. $BP_{ND} + 1$ values for KO and AN mice were significantly higher than DVR values for both the thalamus and midbrain; however, these mice display very low binding of ligand.

To test the reliability of the Python solver for the 2TCM fitting, simulations were performed on the 2-FA and Nifene PET data. Using a mix of male and female mice from the WT, KO, and AN groups, artificial Gaussian noise was applied to the TACs of the thalamus, cerebellum and left ventricle. The noise-induced TACs were then fit by the 2TCM and estimates of the rate constants and binding potential values were derived and compared to the true values derived from the noise-free data. For all groups of mice imaged with 2-FA, the true estimates of BP_{ND}, K_1, k_2, k_3, and k_4 fell within the 25th and 75th percentiles of the simulated values. These findings suggest that the Python solver provides stable estimates of the radioligand rate constants for 2-FA. For Nifene, the true estimates of BP_{ND} fell within the 25th and 75th percentiles of the simulated values for all groups of mice; however, estimates of K_1 and k_2 were underestimated and k_3 and k_4 were overestimated for the WT group only. Since the Nifene TACs were well approximated by the 1TCM, the 2TCM fit had higher levels of uncertainty affiliated with the outcome measures. This uncertainty coupled with the slow input function kinetics resulting from the IP injection likely resulted in the poor estimation of the rate constants for Nifene. Future work will evaluate the 2TCM fit with 2-FA and Nifene delivered via IV injection to improve the ligand kinetics.

Limitations to the Study

Limitations to the current study include not performing arterial sampling on the animals to confirm the left ventricle blood curve, not measuring for potential blood metabolites, which may influence the left ventricle radioactivity curve, and not exploring other brain tissue reference regions (such as the corpus collosum) to compare against the left ventricle blood curve due to the small size of the mouse brain and limited resolution of the PET scanner. While these corrections were not performed, our rate constant estimates were comparable to studies performed with the same radioligands in nonhuman primates [26,27], providing confidence that these results are suitable for exploratory analyses in mouse models of nicotine addiction. To further validate the use of a left ventricle image-derived

input function, future studies incorporating arterial sampling through cannulation should be performed for comparison.

4. Materials and Methods

4.1. Animals

For 2-FA PET, 5 male and 5 female wild type (WT) mice, 8 male and 3 female β2 nAChR knockout (KO) mice, and 3 male and 3 female acute nicotine-treated (AN) mice were imaged. For Nifene PET, 7 male and 5 female WT mice, 5 male and 2 female KO mice, and 2 male and 2 female AN mice were imaged. The male and female KO mice and their WT littermates were generated in house by breeding a heterozygous pair on the C57BL/6J background purchased from the Jackson Lab (Bar Harbor, ME, USA) [34]. Additional male and female WT mice at the same age were purchased directly from the Jackson lab and used in the same manner as the WT littermates. Animals were housed in The University of Chicago Animal Research Resources Center. The Institutional Animal Care and Use Committee of the University of Chicago, in accordance with National Institutes of Health guidelines, approved all animal procedures. Mice were maintained at 22–24 °C on a 12:12-h light–dark cycle and provided food (standard mouse chow) and water ad libitum. All mice were 3–10 months old.

4.2. Radioligand Syntheses

Syntheses of both [^{18}F]2-FA and [^{18}F]Nifene were carried out at the Cyclotron Facility of The University of Chicago (Chicago, IL, USA). 2-FA was synthesized from the commercially available precursor, 2-TMA-A85380 (American Biochemicals Inc., College Station, TX, USA). Nifene was synthesized from the precursor N-BOC-nitroNifene. An IBA Synthera V2 automatic synthesis module (IBA, Louvain-la-Neuve, Belgium) equipped with Synthera preparative HPLC was used for the radiolabeling and purification inside a Comecer hot cell. The radiochemical yield of 2-FA was 34% (decay corrected, based on HPLC analysis of the crude product) with molar activities >111 GBq/μmol and radiochemical purity >99%. The radiochemical yield of Nifene was 6.3% (decay corrected) with molar activities >111 GBq/μmol and radiochemical purity >99%.

4.3. PET/CT Imaging

The imaging protocols were designed based on previous reports for 2-FA and Nifene [35]. An intraperitoneal (IP) catheter was placed at the lower right abdominal area of each mouse before imaging. The animal was then placed into the β-Cube preclinical microPET imaging system (Molecubes, Gent, Belgium) in a small animal holder. The ligand was delivered in 200 μL isotonic saline via the IP catheter and followed with addition of 100 μL of fresh saline. For AN mice, 0.5 mg/kg body weight of nicotine was injected IP 15 min before radioligand injection. Whole-body imaging was acquired with a 133 mm × 72 mm field of view (FOV) and an average spatial resolution of 1.1 mm at the center of the FOV [36]. List-mode data were recorded for 180 min for 2-FA and 60 min for Nifene followed by a reference CT image on the X-Cube preclinical microCT imaging system (Molecubes, Gent, Belgium). The images were reconstructed using an OSEM reconstruction algorithm that corrected for attenuation, randoms, and scatter with an isotropic voxel size of 400 μm. The re-binned frame rate for 2-FA was 10 × 60 s–17 × 600 s and the frame rate for Nifene was 12 × 10 s–18 × 60 s–8 × 300s. CT images were reconstructed with a 200 μm isotropic voxel size and used for anatomic co-registration, scatter correction, and attenuation correction. Animals were maintained under 1–2% isoflurane anesthesia in oxygen during imaging. Respiration and temperature were constantly monitored and maintained using the Molecubes monitoring interface and a Small Animal Instruments (SAII Inc., Stoney Brook, NY, USA) set up. All animals survived the imaging session.

4.4. Image Quantification

For each mouse imaged with 2-FA or Nifene, all PET frames were averaged and coregistered with the anatomical CT using VivoQuant (Invicro, Boston, MA, USA). The resulting transformations were then applied to each individual PET image frame to align the PET with the CT. Brain regional analysis was performed using a 3-dimensional mouse brain atlas available through VivoQuant, which is based on the Paxinos–Franklin atlas registered to a series of high-resolution magnetic resonance images with 100 μm near isotropic data that has been applied in other studies [37–39]. The brain atlas was warped into the CT image space and used for volume of interest (VOI) extraction of the whole brain, cerebellum, thalamus, and midbrain from the PET images. Regional radioactivity concentrations were converted into standardized uptake values (SUVs) by normalizing the signal by the injected dose of the radioligand and the body weight of the animal. In addition, a spherical VOI was hand-drawn over the left ventricle of the heart to act as an image-derived input function for the kinetic modeling analyses.

4.5. Radioligand Kinetic Modeling

Details on the parameters and methodology of implementing the two-tissue compartmental model (2TCM) are described fully in Appendix A. Using radioactivity time–activity curves (TACs) for all mice with the left ventricle TAC as an input function, the 2TCM was fit to the data to solve for the rate constants using an in-house Python software (Spyder v5.1.5). To test the validity of the Python software, the 2TCM was also applied to the data using the built-in solver provided through the π.PMOD software (v3.8). Taking the ratio of k_3 and k_4 resulted in an estimate of the binding potential (BP_{ND}), which was determined for the thalamus, midbrain, and cerebellum. Previous imaging studies of 2-FA and Nifene utilized the distribution volume ratio (DVR) as the outcome measure of specific binding, which is related to BP_{ND} via the following formula:

$$\text{DVR} = BP_{ND} + 1, \tag{1}$$

For the current study, the DVR was determined for the thalamus and midbrain using Logan graphical analysis [33] with the cerebellum acting as a tissue reference region. Using the concentration TACs generated from the VOIs from the VivoQuant brain atlas, a simplified reference tissue model (SRTM) [40] was used to compute the k_2' value for each region. Then, a Logan plot was created, and the slope used as the DVR.

4.6. 2TCM Simulations

To validate the repeatability of the in-house Python solver for the 2TCM, the 2TCM was solved for a series of simulated 2-FA and Nifene data. Details on the simulation methodology are described fully in Appendix A. For both 2-FA and Nifene, independently, regional TACs were taken from a single WT, KO, and AN mouse, and the 2TCM was used to determine the true values for the parameters K_1, k_2, k_3, and k_4. For each time point of the TAC, artificial noise was applied to the radioactivity concentration value with a noise level of 0.2 (noise standard deviation relative to the amplitude) such that the noise level was proportional to the amplitude/time duration. The 2TCM fit was then applied to the noise-induced thalamus and cerebellum TACs using the noise-induced left ventricle TAC as the input function. This process was repeated over 50 iterations for each mouse and radioligand. The parameters for the initial guess for each variable ranged as follows: K_1, k_2, k_3, k_4 = 0.0001–5, and v_p = 0.0001–0.3. Values for K_1, k_2, k_3, k_4, and BP_{ND} were then compared against the true values derived for each mouse.

4.7. Statistical Analyses

All statistical analyses were performed using R v3.0 (The R Project for Statistical Computing). Normality of the data was assessed using the Shapiro–Wilk test. For WT, AN, and KO mice imaged with 2-FA or Nifene, the PET values did not significantly deviate from

the normal distribution (all $p > 0.05$). Peak SUVs (max SUV across entire scan duration) and the mean SUVs from the final 30 min image frames of the left ventricle were compared between WT, KO, and AN mice using analysis of variance (ANOVA). For 2-FA and Nifene independently, K_1 values from the thalamus and midbrain were compared between WT, KO, and AN mice using ANOVA with post hoc Tukey's HSD test for multiple comparisons. The ANOVA and post hoc tests were then repeated for k_2, k_3, k_4, and BP_{ND} values. For all ANOVA analyses, effect sizes are presented as η^2 with 95% CIs. For both radioligands, the 2TCM rate constants from the thalamus and midbrain determined from the in-house Python solver were directly compared to the rate constants determined from PMOD for the WT, KO, and AN mice, independently using paired samples t-tests. $BP_{ND} + 1$ values determined from the 2TCM fit (left ventricle input function) were then directly compared with DVR values from Logan analysis (cerebellum reference tissue) using paired samples t-tests.

5. Conclusions

In summary, these exploratory results show that use of an image-derived input function is suitable for quantification of 2-FA and Nifene PET data in the study of mouse models of nicotine addiction. Consistent with the previous rodent work performed with these radioligands, both 2-FA and Nifene display low levels of specific binding in the cerebellum, further emphasizing the need for analyses using an arterial input function to better estimate $\alpha 4 \beta 2R$ density. Due to the similarity in structure and kinetics of 2-FA and Nifene to varenicline and nicotine, these radioligands are ideal for studying the underlying mechanisms of nicotine addiction and smoking cessation in vivo.

Author Contributions: Conceptualization, W.N.G., J.M., and C.-T.C.; Formal analysis, M.Z., C.-M.K., H.J.Z., H.-M.T., and E.T.; Funding acquisition, W.N.G., J.M., and C.-T.C.; Writing—original draft, M.Z. and C.-M.K.; Writing—review and editing, M.Z., C.-M.K., H.J.Z., H.-M.T., N.H., S.M., E.T., M.B., R.F., A.K., W.N.G., J.M., and C.-T.C. All authors have read and agreed to the published version of the manuscript.

Institutional Review Board Statement: The Institutional Animal Care and Use Committee of the University of Chicago, in accordance with National Institutes of Health guidelines, approved all animal procedures. All studies were carried out in compliance with the ARRIVE guidelines. The project identification code is Animal Care and Use Protocol #72327, approved on 6 June 2022 by The Institutional Animal Care and Use Committee of the University of Chicago.

Informed Consent Statement: Not applicable.

Data Availability Statement: Data can be made available upon request.

Conflicts of Interest: The authors declare no conflict of interest.

Appendix A

The two-tissue compartmental model (2TCM) is described by the following first order ordinary differential equations:

$$\dot{C}_{ND}(t) \; = \; K_1 * C_P(t) - (k_2 + k_3) * C_{ND}(t) + k_4 * C_S(t), \tag{A1}$$

$$\dot{C}_S(t) \; = \; k_3 * C_{ND}(t) - k_4 * C_S(t), \tag{A2}$$

where $C_{ND}(t)$ and $C_S(t)$ are the concentration of the PET ligand in the non-displaceable and specifically bound compartments, respectively, and $C_P(t)$ is the concentration of PET ligand

in the plasma compartment. K_1, k_2, k_3, and k_4 are the rate constants of PET ligand transport between the compartments. Solving Equations (A1) and (A2) yields $C_t(t) = h(t) \star C_p(t)$ where the response function $h(t)$ is given by [41]

$$h(t) = K_1\left(\phi_1 e^{-\theta_1 t} + \phi_2 e^{-\theta_2 t}\right) \tag{A3}$$

with

$$
\begin{aligned}
\theta_1 &= (k_2 + k_3 + k_4 + \Delta)/2 \\
\theta_2 &= (k_2 + k_3 + k_4 - \Delta)/2 \\
\phi_1 &= (\theta_1 - k_3 - k_4)/\Delta \\
\phi_2 &= -(\theta_2 - k_3 - k_4)/\Delta \\
\Delta &= \sqrt{(k_2 + k_3 + k_4)^2 - 4k_2 k_4}
\end{aligned}
\tag{A4}
$$

Therefore, $C_t(t)$ is determined by the rate constants and $C_P(t)$. It can be checked that $0 \le \phi_1, \phi_2 \le 1$ and $\phi_1 + \phi_2 = 1$. Given the TAC for a VOI, the rate constants and v_P for this VOI are the weighted least-squares solution given by:

$$\hat{K}_1, \hat{k}_2, \hat{k}_3, \hat{k}_4, \hat{v}_p = argmin_{K_1,k_2,k_3,k_4,v_p} \sum_{i=0}^{n-1} \sigma_i^{-2} (C_{PET}(t_i) - (1-v_P)C_t(t_i) - v_P C_P(t_i))^2, \tag{A5}$$

where t_i is the mid-time of the ith time frame and $\sigma_i^2 = var\{C_{PET}(t_i)\}$. By setting $k_3 = k_4 = 0$, the above also yields solutions for the one-tissue compartmental model (1TCM) parameters K_1, k_2 and v_p.

Within a scaling factor, the variance σ_i^2 is estimated as follows. Let y_{ij} denote the PET intensity value before decay correction where I and j identify the image voxel and time frame, respectively, and $\langle y_{ij}\rangle_{j:VOI}$ the average of y_{ij} for voxels in a VOI. Then, $C_{PET}(t_i) = (ca_i/\Delta t_i)\langle y_{ij}\rangle_{j:VOI}$ where c is a factor for converting the image intensity to a quantity with a physical unit (e.g., radioactivity concentration), a_i is the correction factor for isotope decay, and Δt_i is the duration of the frame. We assume $var\{y_{ij}\} \propto E\{y_{ij}\}$. Therefore,

$$\sigma_i^2 \propto \left(\frac{ca_i}{\Delta t_i}\right)^2 \langle E\{y_{ij}\}\rangle_{j:VOI} \propto \left(\frac{ca_i}{\Delta t_i}\right)^2 \langle y_{ij}\rangle_{j:VOI} \propto \left(\frac{a_i}{\Delta t_i}\right) C_{PET}(t_i). \tag{A6}$$

Let $C'_{PET}(t_i) = c\langle y_{ij}\rangle_{j:VOI}/\Delta t_i$ be the TAC before decay correction. Similarly, we obtain $var\{C'_{PET}(t_i)\} \propto C'_{PET}(t_i)/\Delta t_i$. Therefore, when adding noise to a simulated noise-free TAC that includes isotope decay, the noise variance was proportional to the TAC value and inversely proportional to the frame duration, with the proportionality constant determined to yield $\beta = \sqrt{\sum_i var\{C'_{PET}(t_i)\}} / \sqrt{\sum_i (C'_{PET}(t_i))^2}$ where β was the desired noise level given by the caller.

2TCM fitting was challenging for the KO and AN animal groups. On observing that, for them, 1TCM could fit the tissue TACs reasonably, we examined and found that there are three situations when the 2TCM becomes approximately 1TCM and hence present ambiguities in the determining the solution. Assuming $k_3 + k_4 \ll k_2$ in Equations (A1) and (A2), we have

$$h(t) \approx K_1\left[\left(1 - \frac{k_3}{k_2}\right)e^{-(k_2+k_3)t} + \left(\frac{k_3}{k_2}\right)e^{-k_4 t}\right] \approx K_1 e^{-(k_2+k_3)t}. \tag{A7}$$

On the other hand, when $k_3 + k_4 \gg k_2$ we get

$$h(t) \approx K_1\left[\frac{k_2 k_3}{(k_3+k_4)^2}e^{-(k_3+k_4)t} + \left(1 - \frac{k_2 k_3}{(k_3+k_4)^2}\right)e^{-(\frac{k_2}{1+BP})t}\right] \approx K_1 e^{-(\frac{k_2}{1+BP})t}. \tag{A8}$$

Both Equations (A7) and (A8) are slightly perturbed exponential functions. The third situation is when $\theta_1 \sim \theta_2$ that occurs $\Delta \sim 0$ and requires $k_3 \sim 0$ and $k_2 \sim k_4$. For the KO and AN groups, we expect $k_3 + k_4 \ll k_2$ and hence the solution given by Equation (A7).

The fitting algorithm, however, could wrongly yield the solution Equation (A8) and obtain large k_3 and k_4 instead. To remove this ambiguity, we note that ϕ_1 is close to 1 in Equation (A7) and close to 0 in Equation (A8). In addition, for both 2FA and Nifene we observe that $k_2 > k_3, k_4$ for the WT group, and one can show $\phi_1 > 1/2$ when $k_2 > k_3, k_4$. Therefore, the fitting algorithm accepts the condition $\phi_{min} \leq \phi_1 \leq \phi_{max}$ where $1/2 < \phi_{min} < \phi_{max} < 1$ for rejecting the solutions with $k_2 \ll k_3 + k_4$. Specifically, we used $0.55 \leq \phi_1 \leq 0.95$ for the WT animal group and $0.85 \leq \phi_1 \leq 0.95$ for the KO and AN groups. However, this condition cannot reject the $\theta_1 \sim \theta_2$ solutions as their ϕ_1 can assume any value. Therefore, as will be explained below, we will also seek to maximize Δ.

Another issue with our experimental data is related to the use of IP injection. Typically, IV injection is used and $C_P(t)$ shows a sharp peak within a few minutes post acquisition. With IP injection, in our data $C_P(t)$ showed a peak at about 10 and 20 min post-acquisition with Nifene and 2FA, respectively, and decreased slowly. With a broader $C_P(t)$, generally a certain change in a rate constant or v_p yields smaller changes in the tissue TACs. Consequently, the fitting result is more sensitive to data noise. The issue is even more challenging with weak binding as the approximate response function in Equation (A7) degenerates to depend on only three parameters $K_1(k_3/k_2)$, $k_2 + k_3$, and k_4. With IP injection, $C_P(t)$ also showed greater inter-subject variabilities. One way to help stabilize the fitting result is to define ranges for the fitting parameters. For this purpose, the in-house algorithm considers $V'_T = (1 - v_p)V_T + v_p$, BP, k_2, k_4, and v_P, where $V_T = (K_1/k_2)(1 + BP)$ and $BP = k_3/k_4$, in place of K_1, k_2, k_3, k_4, and v_P because, as will be described below, we can define ranges for V'_T and BP.

The in-house algorithm began with a wide range $R(x)$ for a parameter x that was unlikely to be violated. Specifically, $R(V'_T) = [1, 20]$, $R(k_2) = R(k_4) = [\epsilon, 5]$, $R(BP) = [\epsilon, 10]$, and $R(v_p) = [\epsilon, 0.3]$ where ϵ is a small number. Subsequently, if another range $R\prime(x)$ was specified for x, the range was updated to $R(x) \cap R'(x)$. The following steps were taken to update the ranges. First, the slope m of the Logan plot, which is an estimate of V'_T, was obtained to define $R\prime(V'_T) = [0.5 m, 2.0 m]$. Next, the tissue TAC was fitted with the 1TCM model based on the parameters K_1, k_2, and v_p. In this case, $R(K_1) = [\epsilon, 5]$ was employed and the updated $R(V'_T)$ was applied to V'_T calculated from the fitting K_1, k_2, and v_p. Using the resulting 1TCM estimates, $R'(V'_T) = [0.5 V'^{*}_T, 2 V'^{*}_T]$ and $R'(k_2) = [0.5 k^*_2, \infty)$, where V'^{*}_T and k^*_2 were the 1TCM solutions, were defined to update the fitting range for V'_T and k_2. Subsequently, we performed 2TCM fitting for the cerebellum VOI that was known to have weak binding so that we could impose a small range for its BP. Specifically, we used $R'(BP) = [0, 2]$. The cerebellum result was then used to obtain $R'(BP)$ for other VOIs by employing the assumption commonly made in the reference-tissue methods: the non-displaceable distribution volume $V_{ND} = K_1/k_2$ is identical for all VOIs. This assumption yielded $(1 + BP)/(1 + BP^r) = V_T/V^r_T$, or $BP = (V_T/V^r_T)(1 + BP^r) - 1$ where V^r_T and BP^r are V_T and BP of the cerebellum. We therefore applied the range condition $R'(BP) = [0.5 BP^*, 2.0 BP^*]$ where BP^* is obtained for the VOI under examination using the above relationship. We also used $R'(v_p) = [0.5 v^*_p, 2.0 v^*_p]$, where v^*_p was the cerebellum value, by assuming all VOIs have similar v_p's. We also set $V_{ND} \geq 1$.

The resulting 2TCM fitting is a nonlinear optimization problem that incorporates range conditions on the optimization parameters and several other constraints. It was solved by employing the basinhopping algorithm provided in the Python scipy package with which the range conditions and constraints could be readily incorporated. As mentioned above, we need to avoid the $\theta_1 \sim \theta_2$ solutions when the 2TCM is approximately 1TCM. This is achieved as follows. The basinhopping algorithm is a two-step global optimizer for functions that may have multiple local minima in their respective "basins". The algorithm uses a local search algorithm to find the local minimum in a basin and random perturbations to jump basins to visit other local minima. We recorded all the local minima found by the algorithm and identified those whose weighted squared errors (WLS) are within 5% of the global minimal WLS. Among these potential solutions, the one having the maximum Δ, so that its θ_1 and θ_2 values are most distinct, was selected as the solution.

References

1. SurgeonGeneral The Health Consequences of Smoking—50 Years of Progress: A Report of the Surgeon General (2014). 2014. Available online: https://stacks.cdc.gov/view/cdc/21569 (accessed on 4 September 2023).
2. Albuquerque, E.X.; Pereira, E.F.; Alkondon, M.; Rogers, S.W. Mammalian Nicotinic Acetylcholine Receptors: From Structure to Function. *Physiol. Rev.* **2009**, *89*, 73–120. [CrossRef] [PubMed]
3. Benwell, M.E.; Balfour, D.J.; Anderson, J.M. Evidence That Tobacco Smoking Increases the Density of (-)-[3H]Nicotine Binding Sites in Human Brain. *J. Neurochem.* **1988**, *50*, 1243–1247. [CrossRef]
4. Breese, C.R.; Marks, M.J.; Logel, J.; Adams, C.E.; Sullivan, B.; Collins, A.C.; Leonard, S. Effect of Smoking History on [3H]Nicotine Binding in Human Postmortem Brain. *J. Pharmacol. Exp. Ther.* **1997**, *282*, 7–13. [PubMed]
5. Marks, M.J.; Burch, J.B.; Collins, A.C. Effects of Chronic Nicotine Infusion on Tolerance Development and Nicotinic Receptors. *J. Pharmacol. Exp. Ther.* **1983**, *226*, 817–825. [PubMed]
6. Schwartz, R.D.; Kellar, K.J. Nicotinic Cholinergic Receptor Binding Sites in the Brain: Regulation In Vivo. *Science* **1983**, *220*, 214–216. [CrossRef]
7. Lewis, A.S.; Picciotto, M.R. High-Affinity Nicotinic Acetylcholine Receptor Expression and Trafficking Abnormalities in Psychiatric Illness. *Psychopharmacology* **2013**, *229*, 477–485. [CrossRef]
8. Vezina, P.; McGehee, D.S.; Green, W.N. Exposure to Nicotine and Sensitization of Nicotine-Induced Behaviors. *Prog. Neuropsychopharmacol. Biol. Psychiatry* **2007**, *31*, 1625–1638. [CrossRef] [PubMed]
9. Brown, D.A.; Garthwaite, J. Intracellular pH and the Distribution of Weak Acids and Bases in Isolated Rat Superior Cervical Ganglia. *J. Physiol.* **1979**, *297*, 597–620. [CrossRef]
10. Zhang, H.J.; Zammit, M.; Kao, C.-M.; Govind, A.P.; Mitchell, S.; Holderman, N.; Bhuiyan, M.; Freifelder, R.; Kucharski, A.; Zhuang, X.; et al. Trapping of Nicotinic Acetylcholine Receptor Ligands Assayed by In Vitro Cellular Studies and In Vivo PET Imaging. *J. Neurosci.* **2023**, *43*, 2–13. [CrossRef]
11. Govind, A.P.; Jeyifous, O.; Russell, T.A.; Yi, Z.; Weigel, A.V.; Ramaprasad, A.; Newell, L.; Ramos, W.; Valbuena, F.M.; Casler, J.C.; et al. Activity-Dependent Golgi Satellite Formation in Dendrites Reshapes the Neuronal Surface Glycoproteome. *eLife* **2021**, *10*, e68910. [CrossRef]
12. Cosgrove, K.P.; Esterlis, I.; Sandiego, C.; Petrulli, R.; Morris, E.D. Imaging Tobacco Smoking with PET and SPECT. In *The Neuropharmacology of Nicotine Dependence*; Balfour, D.J.K., Munafò, M.R., Eds.; Current Topics in Behavioral Neurosciences; Springer International Publishing: Cham, Switzerland, 2015; pp. 1–17. ISBN 978-3-319-13482-6.
13. Lundqvist, H.; Nordberg, A.; Hartvig, P.; Långström, B. (S)-(-)-[11C]Nicotine Binding Assessed by PET: A Dual Tracer Model Evaluated in the Rhesus Monkey Brain. *Alzheimer Dis. Assoc. Disord.* **1998**, *12*, 238–246. [CrossRef]
14. Mazière, M.; Delforge, J. PET Imaging of [11C]Nicotine: Historical Aspects. In *Brain Imaging of Nicotine and Tobacco Smoking*; NPP Books: Ann Arbor, MI, USA, 1995; pp. 13–28.
15. Sihver, W.; Nordberg, A.; Långström, B.; Mukhin, A.G.; Koren, A.O.; Kimes, A.S.; London, E.D. Development of Ligands for In Vivo Imaging of Cerebral Nicotinic Receptors. *Behav. Brain Res.* **2000**, *113*, 143–157. [CrossRef] [PubMed]
16. Horti, A.; Ravert, H.T.; London, E.D.; Dannals, R.F. Synthesis of a Radiotracer for Studying Nicotinic Acetylcholine Receptors: (+/−)-Exo-2-(2-[18F]Fluoro-5-Pyridyl)-7-Azabicyclo [2.2.1]Heptane. *J. Label. Compd. Radiopharm.* **1996**, *38*, 355–365. [CrossRef]
17. Chefer, S.I.; London, E.D.; Koren, A.O.; Pavlova, O.A.; Kurian, V.; Kimes, A.S.; Horti, A.G.; Mukhin, A.G. Graphical Analysis of 2-[18F]FA Binding to Nicotinic Acetylcholine Receptors in Rhesus Monkey Brain. *Synapse* **2003**, *48*, 25–34. [CrossRef] [PubMed]
18. Mukherjee, J.; Lao, P.J.; Betthauser, T.J.; Samra, G.K.; Pan, M.-L.; Patel, I.H.; Liang, C.; Metherate, R.; Christian, B.T. Human Brain Imaging of Nicotinic Acetylcholine A4β2* Receptors Using [18F]Nifene: Selectivity, Functional Activity, Toxicity, Aging Effects, Gender Effects, and Extrathalamic Pathways. *J. Comp. Neurol.* **2018**, *526*, 80–95. [CrossRef] [PubMed]
19. Vaupel, D.B.; Stein, E.A.; Mukhin, A.G. Quantification of A4β2* Nicotinic Receptors in the Rat Brain with microPET® and 2-[18F]F-A-85380. *NeuroImage* **2007**, *34*, 1352–1362. [CrossRef]
20. Zanotti-Fregonara, P.; Chen, K.; Liow, J.-S.; Fujita, M.; Innis, R.B. Image-Derived Input Function for Brain PET Studies: Many Challenges and Few Opportunities. *J. Cereb. Blood Flow. Metab.* **2011**, *31*, 1986–1998. [CrossRef]
21. Ferl, G.Z.; Zhang, X.; Wu, H.-M.; Kreissl, M.C.; Huang, S.-C. Estimation of the 18F-FDG Input Function in Mice by Use of Dynamic Small-Animal PET and Minimal Blood Sample Data. *J. Nucl. Med.* **2007**, *48*, 2037–2045. [CrossRef]
22. Tantawy, M.N.; Peterson, T.E. Simplified [18F]FDG Image-Derived Input Function Using the Left Ventricle, Liver, and One Venous Blood Sample. *Mol. Imaging* **2010**, *9*, 76–86. [CrossRef]
23. Hernandez, A.M.; Huber, J.S.; Murphy, S.T.; Janabi, M.; Zeng, G.L.; Brennan, K.M.; O'Neil, J.P.; Seo, Y.; Gullberg, G.T. Longitudinal Evaluation of Left Ventricular Substrate Metabolism, Perfusion, and Dysfunction in the Spontaneously Hypertensive Rat Model of Hypertrophy Using Small-Animal PET/CT Imaging. *J. Nucl. Med.* **2013**, *54*, 1938–1945. [CrossRef]
24. Weinberg, I.N.; Huang, S.C.; Hoffman, E.J.; Araujo, L.; Nienaber, C.; McKay, M.G.; Dahlbom, M.; Schelbert, H. Validation of PET-Acquired Input Functions for Cardiac Studies. *J. Nucl. Med.* **1988**, *29*, 241–247. [PubMed]
25. Dunnwald, L.K.; Doot, R.K.; Specht, J.M.; Gralow, J.R.; Ellis, G.K.; Livingston, R.B.; Linden, H.M.; Gadi, V.K.; Kurland, B.F.; Schubert, E.K.; et al. PET Tumor Metabolism in Locally Advanced Breast Cancer Patients Undergoing Neoadjuvant Chemotherapy: Value of Static versus Kinetic Measures of Fluorodeoxyglucose Uptake. *Clin. Cancer Res.* **2011**, *17*, 2400–2409. [CrossRef] [PubMed]

26. Hillmer, A.T.; Wooten, D.W.; Slesarev, M.S.; Ahlers, E.O.; Barnhart, T.E.; Murali, D.; Schneider, M.L.; Mukherjee, J.; Christian, B.T. PET Imaging of A4β2* Nicotinic Acetylcholine Receptors: Quantitative Analysis of 18F-Nifene Kinetics in the Nonhuman Primate. *J. Nucl. Med.* **2012**, *53*, 1471–1480. [CrossRef] [PubMed]

27. Hillmer, A.T.; Wooten, D.W.; Slesarev, M.S.; Ahlers, E.O.; Barnhart, T.E.; Schneider, M.L.; Mukherjee, J.; Christian, B.T. Measuring A4β2* Nicotinic Acetylcholine Receptor Density In Vivo with [18F]Nifene PET in the Nonhuman Primate. *J. Cereb. Blood Flow. Metab.* **2013**, *33*, 1806–1814. [CrossRef] [PubMed]

28. Allen, D.D.; Lockman, P.R.; Roder, K.E.; Dwoskin, L.P.; Crooks, P.A. Active Transport of High-Affinity Choline and Nicotine Analogs into the Central Nervous System by the Blood-Brain Barrier Choline Transporter. *J. Pharmacol. Exp. Ther.* **2003**, *304*, 1268–1274. [CrossRef] [PubMed]

29. Deuther-Conrad, W.; Patt, J.T.; Lockman, P.R.; Allen, D.D.; Patt, M.; Schildan, A.; Ganapathy, V.; Steinbach, J.; Sabri, O.; Brust, P. Norchloro-Fluoro-Homoepibatidine (NCFHEB)—A Promising Radioligand for Neuroimaging Nicotinic Acetylcholine Receptors with PET. *Eur. Neuropsychopharmacol.* **2008**, *18*, 222–229. [CrossRef]

30. Govind, A.P.; Vallejo, Y.F.; Stolz, J.R.; Yan, J.Z.; Swanson, G.T.; Green, W.N. Selective and Regulated Trapping of Nicotinic Receptor Weak Base Ligands and Relevance to Smoking Cessation. *eLife* **2017**, *6*, e25651. [CrossRef]

31. Lippiello, P.M.; Sears, S.B.; Fernandes, K.G. Kinetics and Mechanism of L-[3H]Nicotine Binding to Putative High Affinity Receptor Sites in Rat Brain. *Mol. Pharmacol.* **1987**, *31*, 392–400.

32. Whiteaker, P.; Sharples, C.G.V.; Wonnacott, S. Agonist-Induced Up-Regulation of A4β2 Nicotinic Acetylcholine Receptors in M10 Cells: Pharmacological and Spatial Definition. *Mol. Pharmacol.* **1998**, *53*, 950–962.

33. Logan, J.; Fowler, J.S.; Volkow, N.D.; Wang, G.-J.; Ding, Y.-S.; Alexoff, D.L. Distribution Volume Ratios without Blood Sampling from Graphical Analysis of PET Data. *J. Cereb. Blood Flow. Metab.* **1996**, *16*, 834–840. [CrossRef] [PubMed]

34. Picciotto, M.R.; Zoli, M.; Léna, C.; Bessis, A.; Lallemand, Y.; Le Novère, N.; Vincent, P.; Pich, E.M.; Brûlet, P.; Changeux, J.P. Abnormal Avoidance Learning in Mice Lacking Functional High-Affinity Nicotine Receptor in the Brain. *Nature* **1995**, *374*, 65–67. [CrossRef]

35. Horti, A.G.; Chefer, S.I.; Mukhin, A.G.; Koren, A.O.; Gündisch, D.; Links, J.M.; Kurian, V.; Dannals, R.F.; London, E.D. 6-[18F]Fluoro-A-85380, a Novel Radioligand for In Vivo Imaging of Central Nicotinic Acetylcholine Receptors. *Life Sci.* **2000**, *67*, 463–469. [CrossRef] [PubMed]

36. Krishnamoorthy, S.; Blankemeyer, E.; Mollet, P.; Surti, S.; Van Holen, R.; Karp, J.S. Performance Evaluation of the MOLECUBES β-CUBE-a High Spatial Resolution and High Sensitivity Small Animal PET Scanner Utilizing Monolithic LYSO Scintillation Detectors. *Phys. Med. Biol.* **2018**, *63*, 155013. [CrossRef] [PubMed]

37. Hesterman, J.; Ghayoor, A.; Novicki, A.; Wang, X.; Cadoret, Y.; Becerra, L.; Gunn, R.; Avants, B. Multi-Atlas Approaches for Image Segmentation across Modality, Species and Application Area. *Konica Minolta Technol. Rep.* **2019**, *16*, 5.

38. Mazur, C.; Powers, B.; Zasadny, K.; Sullivan, J.M.; Dimant, H.; Kamme, F.; Hesterman, J.; Matson, J.; Oestergaard, M.; Seaman, M.; et al. Brain Pharmacology of Intrathecal Antisense Oligonucleotides Revealed through Multimodal Imaging. *JCI Insight* **2019**, *4*, e129240. [CrossRef]

39. Slavine, N.V.; Kulkarni, P.V.; McColl, R.W. Iterative Image Processing for Early Diagnostic of Beta-Amyloid Plaque Deposition in Pre-Clinical Alzheimer's Disease Studies. *J. Appl. Bioinforma Comput. Biol.* **2017**, *6*, 134. [CrossRef]

40. Lammertsma, A.A.; Hume, S.P. Simplified Reference Tissue Model for PET Receptor Studies. *NeuroImage* **1996**, *4*, 153–158. [CrossRef]

41. Gunn, R.N.; Gunn, S.R.; Cunningham, V.J. Positron Emission Tomography Compartmental Models. *J. Cereb. Blood Flow. Metab.* **2001**, *21*, 635–652. [CrossRef]